Supplementary Information (SI) for Chemical Science.
This journal is © The Royal Society of Chemistry 2025

Structural Disorder as a Key to Photoprotection in Eumelanin Multimers

Kavya Vinod[a], Diana Thomas[a] and Mahesh Hariharan*[a]

[a]School of Chemistry, Indian Institute of Science Education and Research Thiruvananthapuram, Vithura, Thiruvananthapuram, Kerala, India 695551

Contents

Section 1: Materials and Methods

All reagents were purchased from commercial suppliers and used without further purification. Ethyl 5,6-dimethoxyindole-2-carboxylate (DMICE), indole-4-boronic acid pinacol ester and indole-2,7-boronic acid pinacol ester were purchased from BLD Pharmatech Pvt. Ltd. DMICE was purified through column chromatography with a mixture of dichloromethane/hexane prior to spectroscopic studies. All the reactions were carried out in oven-dried glassware before use. Standard gastight syringes and septa were used in the process. Standard purification techniques for drying and distillation were used for all the solvents involved in characterization. Column chromatography was performed using silica gel (80-200 mesh). Yields refer to spectroscopically homogenous substances. Melting points were obtained using a capillary melting point apparatus. High resolution mass spectra (HRMS) were recorded on Thermo Scientific Q mass spectrometer. ^{1}H and ^{13}C NMR spectra were measured on a 500 MHz Bruker Advance DPX spectrometer using 1,1,1,1-tetramethyl silane (TMS) as the internal standard. Steady-state photophysical measurements in solution were carried out in a cuvette of 1 cm path length. Absorption spectra were recorded on a Shimadzu UV-3600 UV-VIS-NIR spectrometer and emission spectra were recorded on Horiba Jobin Yvon Fluorolog spectrometer. The UV-vis absorption spectra in the solution state were measured using the transmission mode. For the thin film measurements, a square quartz substrate was cleaned and 1 mM sample solutions in chloroform were uniformly drop casted. The films were dried in vacuum and stored in a nitrogen atmosphere prior to the experiments. The diffuse-reflectance spectra of the thin films were measured and the corresponding Kubelka-Munk transformed absorption spectra were calculated using *UVProbe* software by Shimadzu. Quantum yields of thin films were measured using an integrating sphere in the Horiba Jobin Yvon Fluorolog spectrometer by exciting at 340 nm for DMICE, 370 nm for DMICE-D and 380 nm for DMICE-T. Fluorescence lifetime measurements were carried out in an IBH picosecond time-correlated single-photon counting (TCSPC) system. The pulse width of the excitation (λ_{exci} = 310 nm) source is determined to be <1 ns and the fluorescence decay profiles were deconvoluted using DAS6.3 and fitted with exponential decay, minimizing the χ^2 values.

Section 1.1: X-ray Crystallography

High quality single crystal of DMICE-D was used for X-ray diffraction experiments. The single crystal was mounted using oil (Infineum V8512) on a glass fiber. All measurements were made on a CCD area detector with graphite monochromated Mo Kα radiation. The data was collected using Bruker APEXII detector and processed using APEX2 from Bruker. The structure was solved by direct method and expanded using Fourier technique. The non-hydrogen atoms were refined anisotropically. Hydrogen atoms were included in idealized positions, but not refined. Their positions were constrained relative to their parent atom using the appropriate HFIX command in SHELX-97.[1] All programs used during the crystal structure analysis are incorporated in the WINGX software.[2] The full validation of CIF and structure factor of DMICE-D were performed using the checkCIF utility and found to be free of major alert levels. Three-dimensional structure visualization and the exploration of the crystal packing of crystals under study were carried out using Mercury 2021.2.0.[3]

Section 1.2: Computational Analysis

All geometry optimisations were carried out in Gaussian 16[4] employing the ωB97XD functional and 6-311G+(d,p) basis set at the DFT level of theory. The long-range Coulombic coupling for DMICE, DMICE-D and DMICE-T were computed using Excitation Energy Transfer (EET) method available in Gaussian 16. Electron and hole transfer coupling values were calculated by employing the CATNIP Tool version 1.9.9.[5] CATNIP uses post-processed Gaussian 16 output files for the respective analyses. The two types of dimers from the crystal packing of DMICE-D are denoted as DMICE-D1 and DMICE-D2. Hole-electron isosurfaces and NTO analysis for the systems were generated using Multiwfn 3.8. Visualization states were rendered using VMD 1.9.3 software. Reorganisation energy of the molecules was computed following the expression $\lambda_M = S_0@S_1 - S_0@S_0$ (*J. Chem. Theory Comput.*, 2023, 19, *8*, 2316–2326), where the reorganization energy is calculated as the energy difference in the S_0 potential energy surfaces at S_1 and S_0 equilibrium geometries.

Section 1.3: Excitonic Coupling Parameters[6,7]

The excitonic coupling within the crystal dimers of DMICE-D (DMICE-D1 and DMICE-D2) was theoretically examined by evaluating the contributions from both long-range and short-range effects. The values of long-range Coulombic coupling originating from the interaction between molecular transition dipole moments is obtained through the transition charge method using TrESP. The point atomic charges (q) for a monomer are obtained by the transition charge from electrostatic potential (TrESP), and the excitonic coupling corresponds to the Coulomb interaction of transition charges of two monomers:

$$J_{Coul} = \frac{1}{4\pi\varepsilon_o} \sum_{i} \sum_{j} \frac{q_i\, q_j}{|r_i - r_j|} \qquad \text{(Equation S1)}$$

where q_i (q_j) represents the transition charge on atom i (atom j) of monomer 1 (monomer 2) in a dimer. Similarly, r_i (r_j) refers to the position vectors of atom i (atom j) of monomer 1 (monomer 2) in a dimer. The TrESP transition charges were obtained from Multiwfn[8] program package.

The short-range exciton coupling stemming from the degree of overlap of wave functions on proximal molecules has a crucial role in defining the excitonic interaction and is determined as,

$$J_{CT} = \frac{-2t_e t_h}{E_{CT} - E_{S_1}} \qquad \text{(Equation S2)}$$

where t_e and t_h are the electron and hole-transfer coupling which depend on the LUMO–LUMO and HOMO–HOMO orbital overlap of the monomers, respectively, E_{CT} is the energy of the charge-transfer state, and E_{S_1} is the energy of first Frenkel exciton state. The total coupling between neighbouring molecules can be represented as,

$$J_{Total} = J_{Coul} + J_{CT} \qquad \text{(Equation S3)}$$

Section 1.4: TheoDORE Analysis[9,10]

The excitations of the different dimers obtained from the crystal structure were analyzed using TheoDORE. We studied dimer systems, where each of the molecule in the non-covalent dimer is considered as a fragment. The parameters used to investigate the excited state characteristics are participation ratio (PR), mean position (POS) of initial orbital (hole) and final orbital (electron), and charge transfer character (CT). The magnitude of PR relates to the number of fragments participating in the excitation; hence, in our investigation, the PR ranges from 1 to 2. POS provides the mean position of hole and electron for a particular excitation. Charge transfer states and delocalized Frenkel states show POS = 1.5. If the Frenkel state is localized on monomer A, then POS = 1, and if localized on monomer B, POS = 2, for a dimer AB. Finally, CT is related to the total weight of configurations where initial and final orbitals are situated on different fragments. A CT value of 1 denotes the presence of a charge-separated state, and CT = 0 refers to Frenkel states.

Section 1.5: Scanning Electron Microscopy

SEM measurements were carried out on FEI Nova NanoSEM 450 (FEG type), drop casting the samples on the flat surface of 400 mesh carbon-coated copper grid (Ted Pella, Inc.) and allowing to evaporate the excess solvent under air in dust free conditions. The sample was further subjected to thin chromium sputtering using JEOL JFC-1100 fine coater to increase the signal/noise ratio. The probing side was inserted into JEOL JSM-5600 LV scanning electron microscope for obtaining the images.

Section 1.6: Transmission Electron Microscopy

TEM measurements were carried out on FEI Tecnai 30 G2 high resolution transmission electron microscope and JEOL 2010 with an accelerating voltage of 100 kV. The samples were prepared by drop casting the solutions on a 400-mesh carbon-coated copper grid (Ted Pella, Inc.) at ambient conditions and allowing the excess solvent to evaporate in dust free conditions. TEM images were obtained without staining.

Section 1.7: Confocal Laser Scanning Microscopy

Confocal imaging was performed using a Nikon Eclipse Ti microscope. Sample solutions (100 µL of 1 mM solutions) were drop-cast onto glass microscope slides and allowed to dry under ambient, dust-free conditions to ensure complete evaporation of the solvent. After drying, the exposed surface was covered with a glass coverslip. Imaging was carried out without the use of external stains, using a 20× objective lens on the Nikon Eclipse Ti.

Section 1.8: Estimation of radiative (k_r) and non-radiative (k_{nr}) rate constants[11]

The radiative and non-radiative rate constants were calculated as follows.

$$\phi_F = \frac{k_r}{k_r + k_{nr}} \qquad \text{(Equation S4)}$$

$$\tau_F = \frac{1}{k_r + k_{nr}} \qquad \text{(Equation S5)}$$

$$k_r = \frac{\phi_F}{\tau_F} \qquad \text{(Equation S6)}$$

where ϕ_F is the fluorescence quantum yield and τ_F is the fluorescence lifetime.

Section 1.9: Femtosecond Transient Absorption (fsTA) Measurement

A Spectra-Physics Mai Tai SP mode-locked laser, with an operating frequency of 86 MHz and emitting light at 800 nm, served as the seed for a Spectra-Physics Spitfire ace regenerative amplifier. The regenerative amplifier operated at a repetition rate of 1 kHz and produced an output energy of 5.5 mJ. A fraction of the amplified output was utilized to generate a 520 nm pump pulse through TOPAS. Simultaneously, the remaining 800 nm pulse underwent an optical delay within an ExciPro pump-probe spectrometer. A sapphire crystal introduced into this path generated a white light continuum, which was then split into two streams, serving as probe and reference pulses. Femtosecond transient absorption spectra of the sample were captured using a dual diode array detector with a detection window of 200 nm and an optical delay of 3.5 ns. Sample solutions housed in a rotating cuvette with a path length of 1.2 mm were employed for recording. To enable accurate deconvolution of the transient absorption data, an instrument response function (IRF) was determined. The IRF, established through a solvent (10% benzene in methanol) two-photon absorption, was approximately 110 fs at around 530 nm. An 80% neutral density filter regulated incident flux on the sample. For the fsTA measurement of the samples, the sample was excited with 320 nm, 200 nJ, and 100 fs pulses. The observed kinetic components were independent of laser intensity, eliminating the possibility of singlet–singlet annihilation. The fstA experiments were performed at the magic angle polarization ~54.7° of the pump.

Section 1.10: Sample preparation for thin film for fsTA analysis:

For the fsTA thin film measurements, a round quartz substrate was cleaned by sequential sonication in deionized water, isopropanol, and acetone for 10 min each and dried under nitrogen. Followingly, 1 mM sample solutions in chloroform were uniformly dropcasted on the quartz substrate. The films were dried in a vacuum and stored in a nitrogen atmosphere prior to the experiments. The magic angle polarization ~54.7°, between pump and probe pulses for the fsTA experiments were used to ensure an isotropic signal of the sample.

Section 1.11: Nanosecond Transient Absorption (nsTA) Measurement

Nanosecond laser flash photolysis experiments were performed on nitrogen-degassed solutions of DMICE-D and DMICE-T prepared in toluene and acetonitrile. The measurements were carried out using an Applied Photophysics LKS-60 laser kinetic spectrometer. Excitation was achieved with the third harmonic output (532 nm, ~10 ns pulse width) of a Quanta Ray INDI-40-10 series pulsed Nd:YAG laser.

Section 1.12: Global Analysis

The fsTA spectra underwent global analyses using Glotaran software. This process involved assessing the instrument time response function and the group velocity dispersion of the white continuum, enabling the computation of decay time constants and dispersion-compensated spectra. The fsTA data were fitted using a sequential A → B → C → GS model. Parallel model was also tested but resulted in poor fits compared to the sequential model, which provided the best description of the observed kinetics. In global analysis of the fsTA data, all wavelengths were simultaneously scrutinized, utilizing a sequential model to generate the time constants associated with specific spectral changes.

Section 1.13: Spectral Plotting and Data Handling

All transient absorption spectra were recorded over two probe windows (~200 nm each) and stitched together to span the visible region. The central probe wavelengths were set to 520 nm for solution samples and 540 nm for film samples, which results in visible spectral discontinuities at the stitching points. For improved visual clarity, fsTA spectra were plotted after smoothing the raw data using Savitzky-Golay over 25 points (OriginLab); this procedure did not alter the spectral dynamics or features, as all quantitative analyses using Glotaran were performed using the raw data.

Section 2: Synthesis and Characterization

Section 2.1: Synthesis

a) DMICE-D: The synthesis procedure follows the reported literature with minor modifications. To a Schlenk tube added XPhosPd G2 (4 mol%, 0.0024 mmol), IDMICE (1 equiv, 0.06 mmol) and indole-4-boronic acid pinacol ester (1.25 equiv, 0.075 mmol), evacuated with vacuum and purged with N_2. 1,4-dioxane (0.66 mL) and 0.5 M K_3PO_4 (3 equiv, 0.18 mmol) were then added to the Schlenk tube. The reaction mixture was heated at 75 °C for 20 h and quenched with the addition of H_2O. The crude mixture was extracted with EtOAc, dried with $MgSO_4$, filtered, and concentrated in vacuo. The product was purified via column chromatography (silica, hexanes: EtOAc: 3:2 to 2:1) to yield off-white powders of DMICE-D (63% yield; off-white solid).

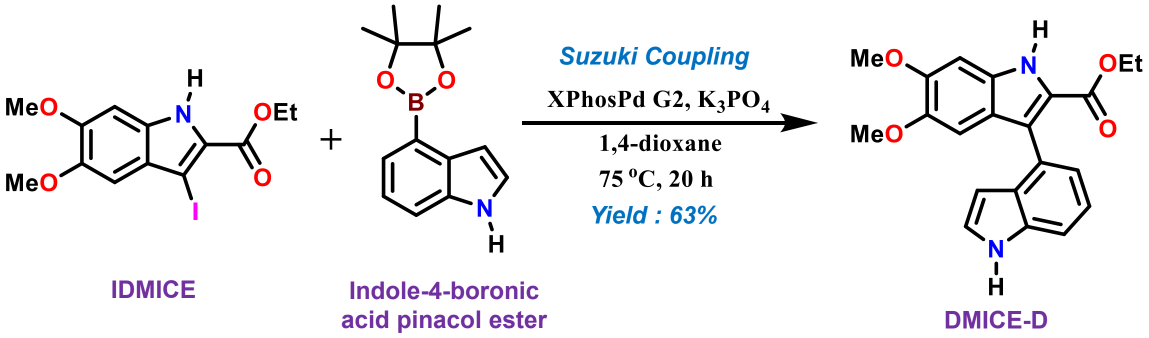

Scheme S1: The reaction scheme for the synthesis of DMICE-D.

b) DMICE-T: To a Schlenk tube that is evacuated and purged with N_2, added XPhosPd G2 (4 mol%, 0.01084 mmol, 0.04 equiv), IDMICE (2.1 equiv, 0.569 mmol) and indole-2,7-boronic acid pinacol ester (1 equiv, 0.271 mmol), evacuated with vacuum and purged with N_2. 1,4-dioxane (6.26 mL) and 0.5 M K_3PO_4 (3 equiv, 0.813 mmol) were then added to the Schlenk tube. The reaction mixture was heated at 75 °C for 20 h and quenched with the addition of H_2O. The crude mixture was extracted with EtOAc, dried with $MgSO_4$, filtered, and concentrated in vacuo. The product was purified via column chromatography (silica, DCM:EtOAc : 100:1) to yield wheatish powders of DMICE-T (25% yield; wheatish solid).

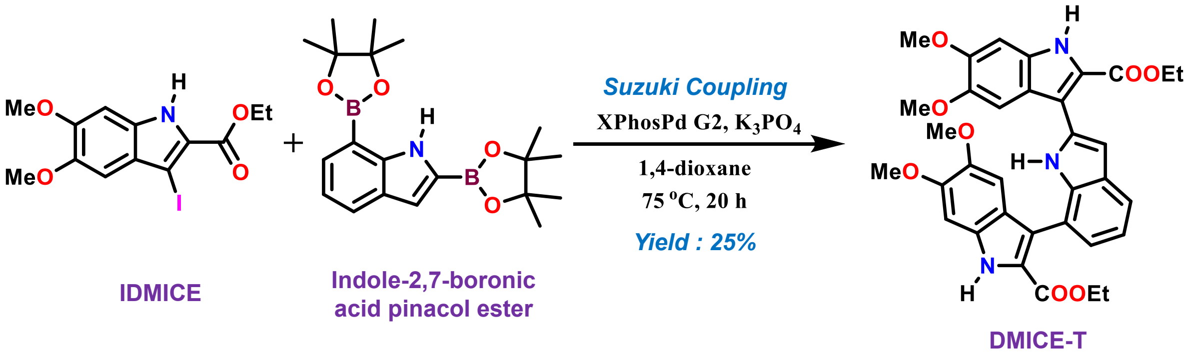

Scheme S2: The reaction scheme for the synthesis of DMICE-T.

Section 2.2: Characterization

a) DMICE-D: ^{1}H NMR (500 MHz, $CDCl_3$, ppm): δ = 8.92 (s, 1H), 8.23 (s, 1H), 7.44 (d, J = 7.8 Hz, 1H), 7.30 (m, 2H), 7.18 (s, 1H), 6.89 (d, J = 14.7 Hz, 2H), 6.31 (s, 1H), 4.14 (m, 2H), 3.97 (s, 3H), 3.75 (s, 3H), 1.00 (t, J = 7.1 Hz, 3H).
^{13}C NMR (125 MHz, $CDCl_3$, ppm): δ = 162.27, 150.41, 146.11, 136.00, 131.01, 128.08, 126.59, 123.90, 123.23, 122.22, 122.19, 121.73, 121.35, 110.28, 103.30, 102.66, 93.63, 60.52, 56.27, 56.24, 13.94.
HRMS (APCI) (m/z): Calculated for $C_{21}H_{21}N_2O_4$ $[M+H]^+$: 365.1496, found: 365.1486 $[M+H]^+$
Melting Point (°C): 129.6 °C

b) DMICE-T: ^{1}H NMR (500 MHz, $CDCl_3$, ppm): δ = 11.25 (s, 1H), 9.13 (s, 1H), 8.78 (s, 1H), 7.74 (d, J = 7.8 Hz, 1H), 7.61 (s, 1H), 7.33 (d, J = 7.1 Hz, 1H), 7.24 (s, 1H), 7.16 (s, 1H), 6.98 (s, 1H), 6.92 (s, 1H), 6.83 (s, 1H), 4.26 (q, J = 7.1 Hz, 2H), 4.10 (m, 1H), 4.04 (s, 3H), 3.99 (dd, J = 10.5, 7.2 Hz, 1H), 3.95 (d, J = 3.1 Hz, 6H), 3.77 (s, 3H), 1.25 (t, J = 6.5 Hz, 3H), 0.76 (t, J = 7.1 Hz, 3H).
^{1}H NMR (500 MHz, $(CD_3)_2SO$, ppm): δ = 11.75 (s, 1H), 11.67 (s, 1H), 11.46 (s, 1H), 7.63 (m, 1H), 7.43 (s, 1H), 7.13 (m, 3H), 6.98 (d, J = 15.3 Hz, 2H), 6.77 (s, 1H), 4.20 (q, J = 6.9 Hz, 2H), 4.03 (dq, J = 14.2, 6.9 Hz, 1H), 3.90 (m, 1H), 3.87 (s, 3H), 3.83 (s, 6H), 3.62 (s, 3H), 1.18 (t, J = 7.0 Hz, 3H), 0.74 (t, J = 7.0 Hz, 3H).
^{13}C NMR (125 MHz, $CDCl_3$, ppm): δ = 162.31, 161.87, 151.05, 150.57, 146.90, 146.43, 135.46, 131.48, 131.35, 131.30, 128.77, 123.96, 122.85, 121.46, 120.16, 120.03, 119.66, 119.51, 119.49, 118.04, 116.69, 103.26, 102.32, 102.06, 93.76, 93.62, 61.55, 60.58, 56.57, 56.31, 56.25, 56.21, 14.36, 13.49.
HRMS (APCI) (m/z): Calculated for $C_{34}H_{32}N_3O_8$ $[M-H]^-$: 610.2195, found: 610.2187 $[M-H]^-$
Melting Point (°C): 239.1 °C

Section 3: Tables

Table S1: Previous works on elucidating the structure-property relationship in eumelanin and eumelanin substructures.

Contributed by	Journal	Methods employed
Buehler and coworkers	***Nat. Commun.***, 2014, *5*, 3859	Molecular dynamics (MD) simulations, DFT
Blancafort and coworker	***Angew. Chem. Int. Ed.,*** 2021, 60, 18800	Density functional theory (DFT)
Hodgkiss and co-worker	***Proc. Natl. Acad. Sci.***, 2022, 119, e2212343119	Time-resolved spectroscopy
Buehler and coworkers	***Chem. Sci.***, 2017, 8, 1631-1641	Molecular dynamics (MD) simulations, DFT
Sundström and coworkers	***J. Am. Chem. Soc.*** 2014, *136*, 11626–11635	Fluorescence spectroscopy
Hariharan, Thomas and coworkers	***Chem. Sci.***, 2024, D4SC05453A	3D-ED, solid state NMR
Hariharan and coworkers	***Current work*,** 2024	Single crystal XRD, Time-resolved spectroscopy, Electron Microscopy

Table S2: Crystallographic data and refinement parameters for DMICE-D.

Parameters	DMICE-D
Formula	$C_{21}H_{20}N_2O_5$
Formula weight	380.39
Colour	Colourless
Crystal system	Monoclinic
Space group, Z	P 21/c, 4
A (Å)	14.018(3)
B (Å)	17.554(3)
C (Å)	7.8113(15)
A (deg)	90
B (deg)	104.941(5)
Γ (deg)	90
Volume, A^3	1857.1(6)
R-factor	6.64
Temp (K)	296
$\text{Density}_{\text{calc}}(\text{Mg/m}^3)$	1.360
No. of reflections collected	31352
Independent reflections	4644
$2\Theta_{\text{MAX}}$ (deg)	28.471
R indices, wR2, (i>2s(i))	0.0664, 0.1446
R indices, wR2 (all data)	0.1613, 0.1789
Goodness of fit	1.025
CCDC number	2389911

Table S3: DFT optimized geometry parameters of DMICE-D computed at different functionals/basis sets.

Functional/basis set	Dihedral angle, ϕ (°) (C6–C7–C14–C25)	Bond angle, θ (°) (O44–C16–O45)	Bond length, x (Å) (C15–C16)
ωb97xd/6-311g+(d,p)	54.49	123.03	1.47
cam-b3lyp/6-311g+(d,p)	57.71	122.76	1.47
b3lyp/6-311g+(d,p)	58.66	122.75	1.48
hseh1pbe/6-311g+(d,p)	54.31	122.79	1.47

Table S4: DFT optimized geometry parameters of DMICE-T computed at different functionals/basis sets.

Functional/basis set	Dihedral angle, ϕ (°) (C16–C10–C8–N7)	Dihedral angle, ϕ (°) (C4–C3–C12–C17)	Bond angle, θ (°) (O32–C31–O33)	Bond length, x (Å) (C13–C31)
ωb97xd/6-311g+(d,p)	39.59	60.11	124.44	1.47
cam-b3lyp/6-311g+(d,p)	38.81	61.76	124.04	1.47
b3lyp/6-311g+(d,p)	38.81	61.76	124.04	1.46
hseh1pbe/6-311g+(d,p)	36.13	60.07	124.12	1.46

Table S5. Vertical excitation energies of DMICE, DMICE-D and DMICE-T computed at the ωb97xd/6-311+g(d,p) level of theory.

DMICE			**DMICE-D**			**DMICE-T**		
State	dE(eV)	f	State	dE(eV)	f	State	dE(eV)	f
S_1	4.205	0.484	S_1	4.225	0.221	S_1	3.880	0.342
S_2	4.320	0.114	S_2	4.339	0.461	S_2	4.141	0.145
S_3	5.319	0.000	S_3	4.767	0.070	S_3	4.317	0.410
S_4	5.486	0.020	S_4	4.858	0.039	S_4	4.449	0.469
S_5	5.536	0.087	S_5	5.117	0.073	S_5	4.503	0.028
S_6	5.737	0.002	S_6	5.388	0.000	S_6	4.603	0.047
S_7	5.859	0.003	S_7	5.460	0.015	S_7	4.868	0.080
S_8	5.966	0.002	S_8	5.503	0.012	S_8	5.023	0.047
S_9	6.270	0.003	S_9	5.536	0.009	S_9	5.140	0.047
S_{10}	6.311	0.000	S_{10}	5.563	0.006	S_{10}	5.330	0.006

Table S6. Solvent-dependent steady-state optical properties of DMICE-D and DMICE-T.

Compound	**Solvent**	**λ_{abs} (nm)**	**λ_{emi} (nm)**	**Φ_{fl} (%)**
DMICE-D	TOL	326	400	27.5
	ACN	325	432	17.5
DMICE-T	TOL	331	425	13.6
	ACN	331	454	4.6

Table S7. Electronic coupling calculated via the excitation energy transfer (EET) method at the cam-b3lyp/6-311g+(d,p) for DMICE-D.

Fragment	**Coulomb (meV)**	**Exact exchange (meV)**	**Exchange correlation (meV)**
1 & 2	0.40	3.36	0.49

Table S8. Electronic coupling calculated via the excitation energy transfer (EET) method at the cam-b3lyp/6-311g+(d,p) for DMICE-T.

Fragment	**Coulomb (meV)**	**Exact exchange (meV)**	**Exchange correlation (meV)**
1 & 2	0.00	1.14	1.67
2 & 3	0.00	-1.34	-0.12
1 & 3	-17.19	0.17	0.00

Table S9. Coulombic and charge transfer coupling values calculated at the cam-b3lyp/6-311g+(d,p) for the identified DMICE-D dimers within the crystal packing.

	Dimer 1	**Dimer 2**
J_{CT} (cm^{-1})	-12.74	9.41
J_{Coul} (cm^{-1})	47.85	54.34
J_{Total} (cm^{-1})	34.71	63.75

Table S10. Vertical excitation energies of nearest triplet states to the S_1 state for DMICE-D and DMICE-T at the ωb97xd/6-311+g(d,p) level of theory.

Compound (S_1 energy)	**Triplet State**	**Energy (eV)**
DMICE-D (S_1 = 4.19 eV)	T_1	2.74
	T_2	3.13
	T_3	3.38
	T_4	4.94
	T_5	4.14
	T_6	4.53
DMICE-T (S_1 = 3.88 eV)	T_1	2.58
	T_2	2.79
	T_3	3.13
	T_4	3.36
	T_5	3.55
	T_6	3.74
	T_7	3.88

Table S11. Summary of decay rate constants of different species (obtained from fsTA and nsTA) for DMICE-D in TOL and ACN.

	Component A	**Component B**	**Component C**
TOL	6.7 ps	2.43 ns	1.2 μs
ACN	3.7 ps	2.18 ns	0.80 μs

Table S12. Summary of decay rate constants of different species (obtained from fsTA and nsTA) for DMICE-T in TOL and ACN.

	Component A	**Component B**	**Component C**
TOL	7.4 ps	0.98 ns	1.3 μs
ACN	3.3 ps	0.34 ns	0.77 μs

Table S13: Comparison of structural and photophysical features of DMICE-based multimers and natural eumelanin.

Property	**DMICE-D / DMICE-T**	**Natural Eumelanin**	**Remarks**
Monomeric Unit	Substituted indole (DMICE)	DHI, DHICA, indolequinones	DMICE retains the indole scaffold with blocking groups to prevent polymerization
Polymerization Tendency	Bench-stable, controlled oligomers	Spontaneous polymerization into heterogeneous polymers	Structural modification stabilizes the molecules
UV-vis Absorption	In UV regime (DMICE-D), till ~420 nm (DMICE-T)	Broad UV-vis-NIR profile	DMICE-T shows modest visible absorption; longer oligomers may extend further
Absorption Profile	Structured, molecule-specific	Broad, featureless	Aggregation and heterogeneity in eumelanin lead to featureless spectra; hard to dissect
Excited-State Lifetime	Ns-μs (monomers), sub–ns (aggregates)	Ps timescale (*Proc. Natl. Acad. Sci. U.S.A.*, 2022, 119, *43*, e2212343119)	Ultrafast internal conversion among neighbouring coupled chromophores
Triplet State Formation	Observed (μs lifetime)	Less likely in polymer though suspected in monomers (*J. Phys. Chem. B* 2009, *37*, 12575–12580)	Heavy-atom-free ISC possible in monomers
Excited state charge-transfer	Sub-ns timescale excited CT states	Sub-ps timescale excited CT states (J. Phys. Chem. Lett. 2024, 15, 13, 3639–3645)	Excited CT states are predominant

Table S14. Comparison of protected (DMICE-based) and unprotected (DHI/DHICA) eumelanin multimers.

Property	**Unprotected DHI/DHICA oligomers** (*J. Phys. Chem. B*, 2012, 116, *44*, 13151; *J. Am. Chem. Soc.*, 2014, 136, *33*, 11626)	**Protected DMICE-based oligomers** (This work)
Chemical stability	Low (prone to oxidative polymerization and in situ photochemical reactions)	High (methyl protection blocks uncontrolled polymerization)
Excited-State Proton Transfer (ESPT)	Observed; contributes to ultrafast fluorescence	Suppressed due to methyl protection
Fluorescence lifetimes (in solution)	Multiexponential: short-lived (ps) + long-lived (ns) components	Predominantly ns components in solution
Fluorescence lifetimes (in aggregates/films)	Unexplored due to fast polymerisation	Multiexponential with emerging ps components (indicative of exciton effects)
Triplet-state formation/ISC	Unexplored due to fast polymerisation	Directly observed and quantified using transient absorption
Exciton effects	Unexplored due to fast polymerisation	Isolated and studied systematically across oligomer length
Interpretability of photophysics	Complicated by overlapping decay pathways and chemical heterogeneity	Mechanistic contributions (e.g., ISC, exciton coupling) isolated and resolved
Experimental tools	Time-resolved fluorescence spectroscopy	Transient absorption (fsTA and nsTA), time-resolved fluorescence spectroscopy, microscopy

Section 4: Figures

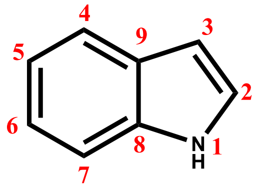

Figure S1: Structure of indole with the numbering of atoms.

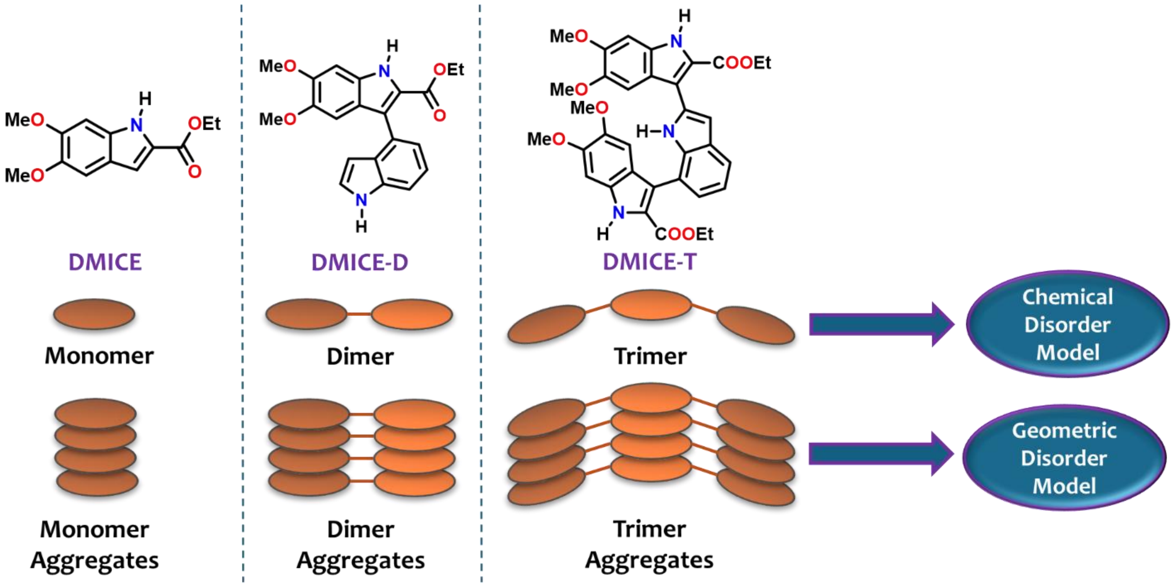

Figure S2: Schematic representation of our approach in understanding the influence of chemical and geometric disorder model through photophysical investigation of model eumelanin oligomers in solution, aggregate and crystalline states.

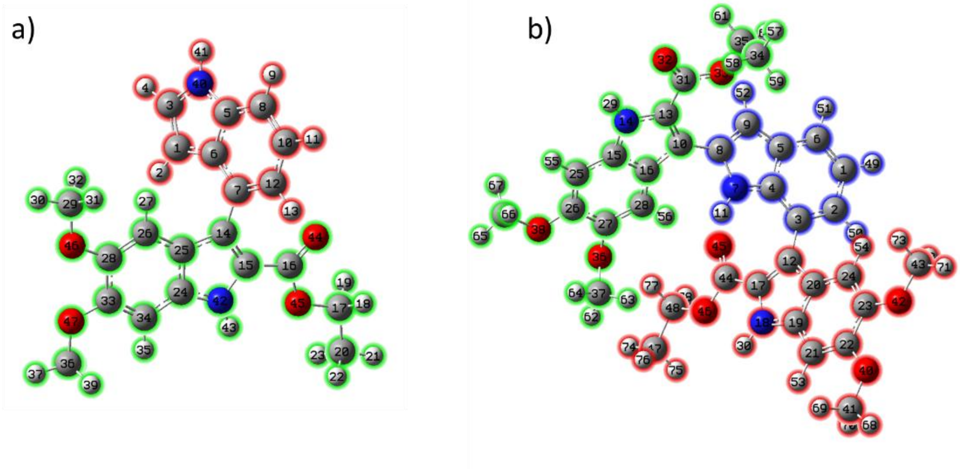

Figure S3: Optimized structure of a) DMICE-D and b) DMICE-T, at the ωb97xd/6-311G+(d,p) level of theory.

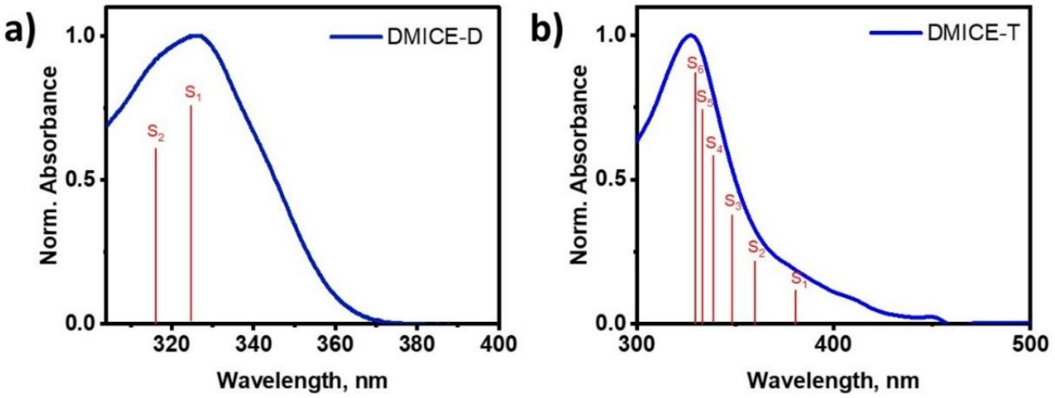

Figure S4: Comparison of experimental UV-vis absorption spectrum of a) DMICE-D and b) DMICE-T with the computed vertical excitation energies (red lines). Note: The vertical excitation energies are computed at the ωb97xd/6-311G+(d,p) level of theory and corrected with respect to the λ_{max} of the experimental absorption.

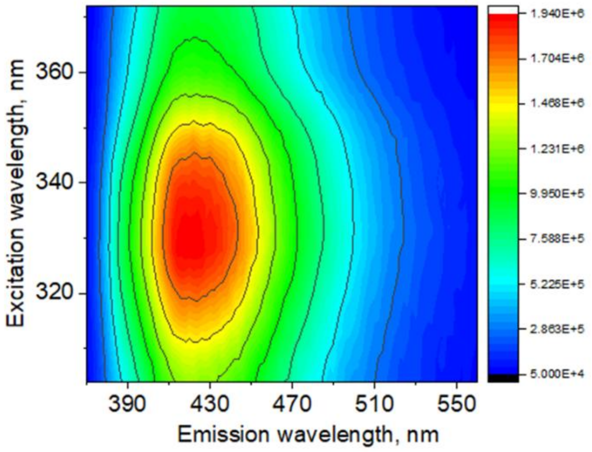

Figure S5: Excitation dependent fluorescence spectra of DMICE-T.

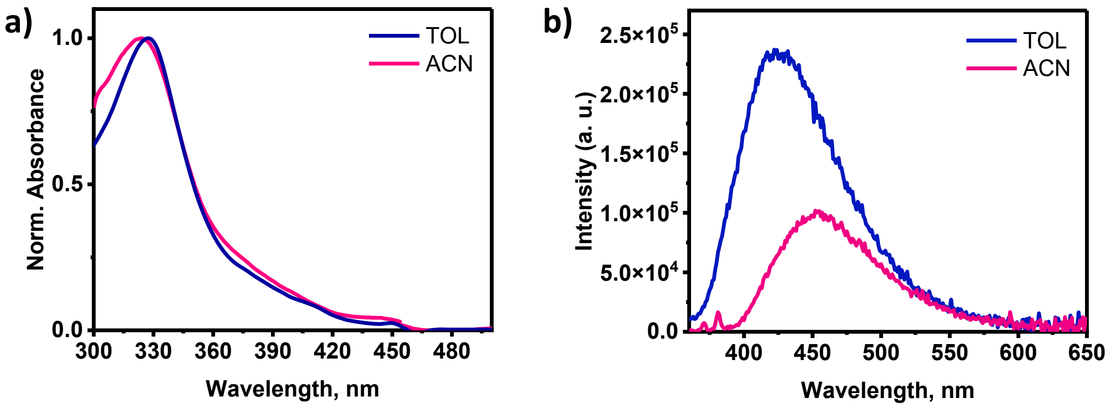

Figure S6: a) UV-vis absorption and b) fluorescence emission spectra of DMICE-T in TOL and ACN.

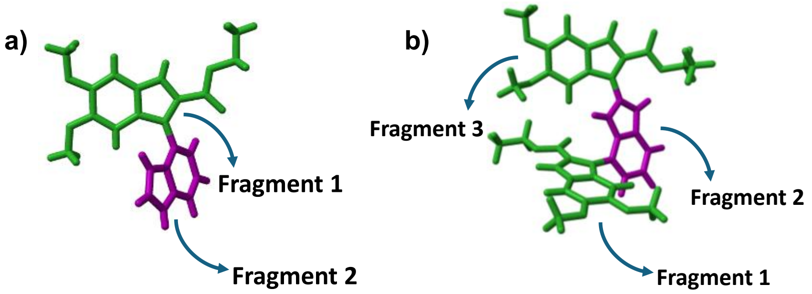

Figure S7: Fragmentation used for computing long-range Coulombic coupling via Electronic Excitation Transfer (EET) method in a) DMICE-D and b) DMICE-T.

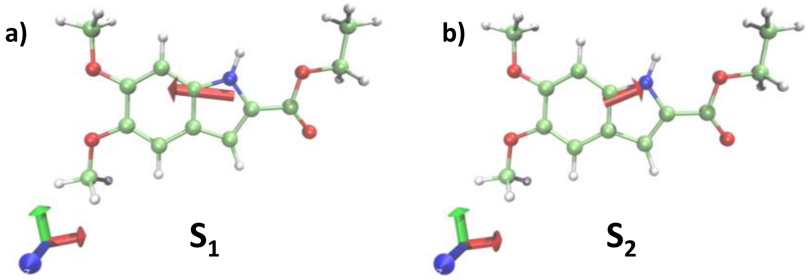

Figure S8: Transition dipole moments for DMICE in a) S_1 state and b) S_2 state.

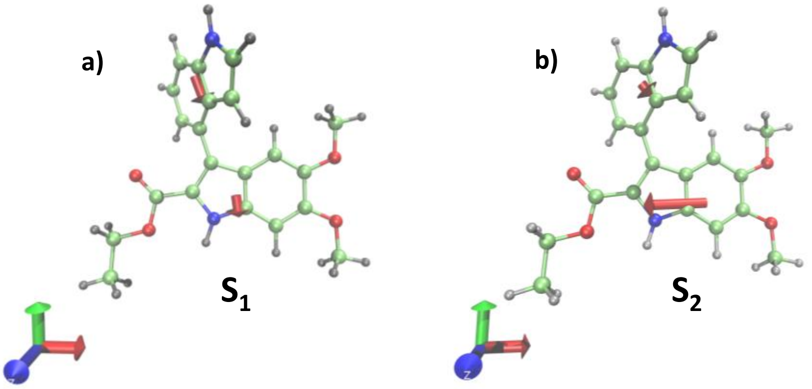

Figure S9: Transition dipole moments for DMICE-D in a) S_1 state and b) S_2 state.

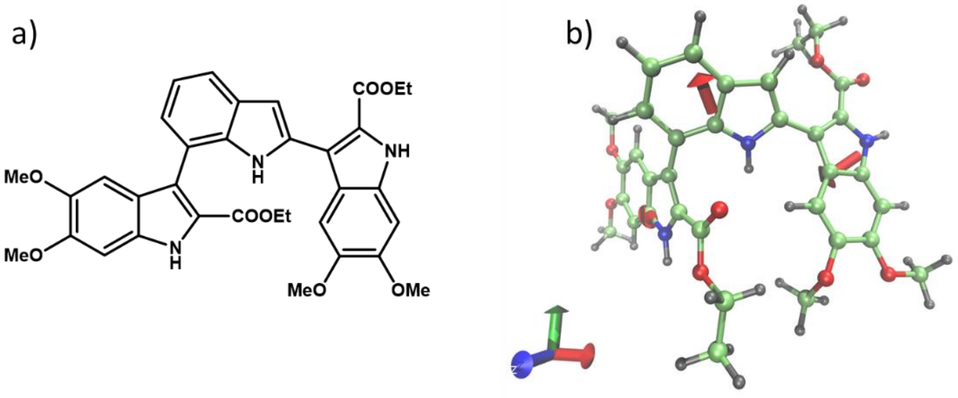

Figure S10: a) Molecular structure and b) transition dipole moments for DMICE-T in S_1 state.

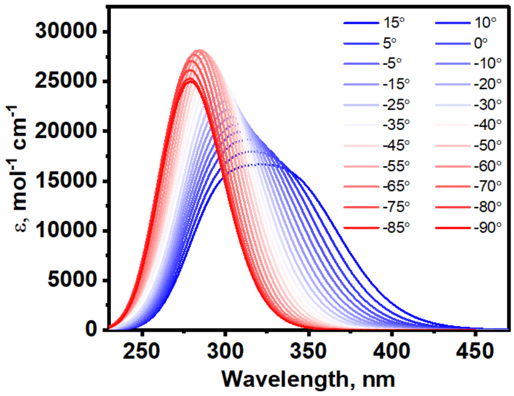

Figure S11: Simulated electronic absorption spectra of DMICE-D upon changing the dihedral angle between the indole units, computed at the ωb97xd/6-311+g(d,p) level of theory.

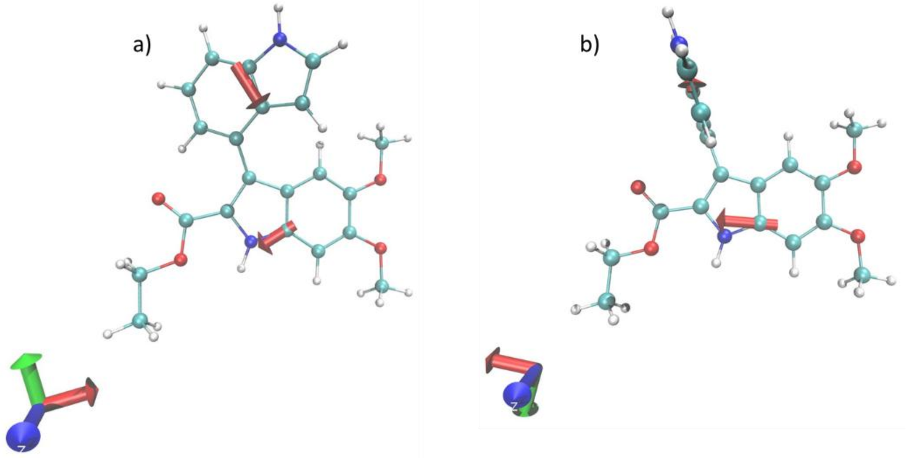

Figure S12: Transition dipole moments for DMICE-D in S_1 state for geometries with inter-fragment torsional angle a) 0° and b) 90°.

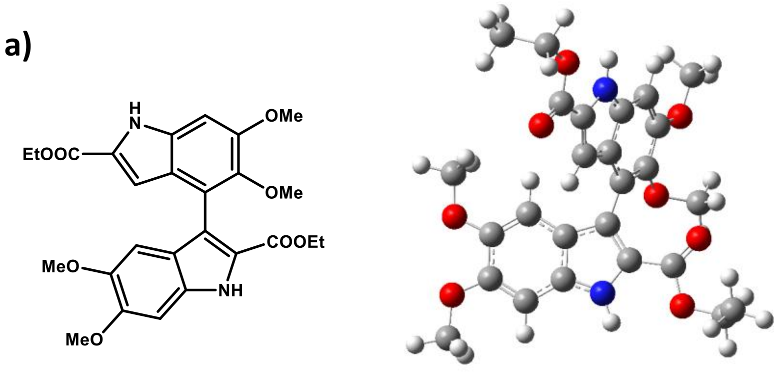

DMICE homo-dimer

S0→S1 = 4.23 eV or 293 nm

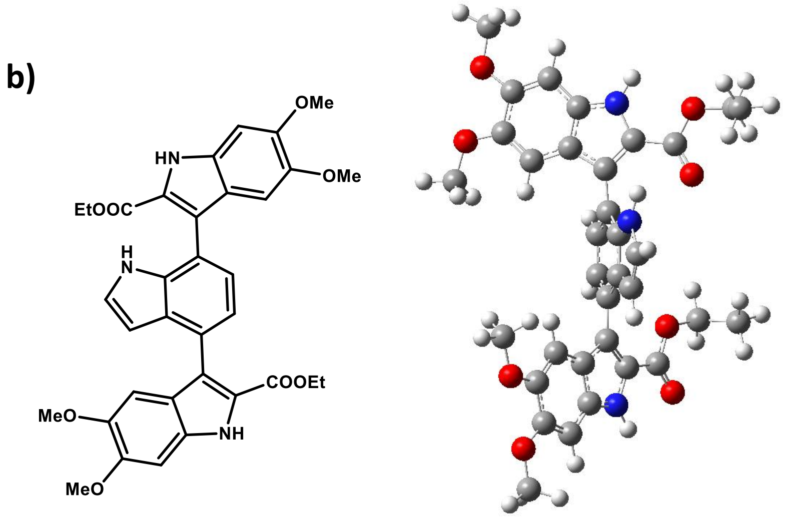

DMICE linear trimer

S0→S1 = 3.98 eV or 311 nm

Figure S13: Optimized geometries and vertical excitation energies of the S_1 state for a) DMICE homo-dimer and b) DMICE linear trimer, computed at the computed at the ωb97xd/6-311+g(d,p) level of theory.

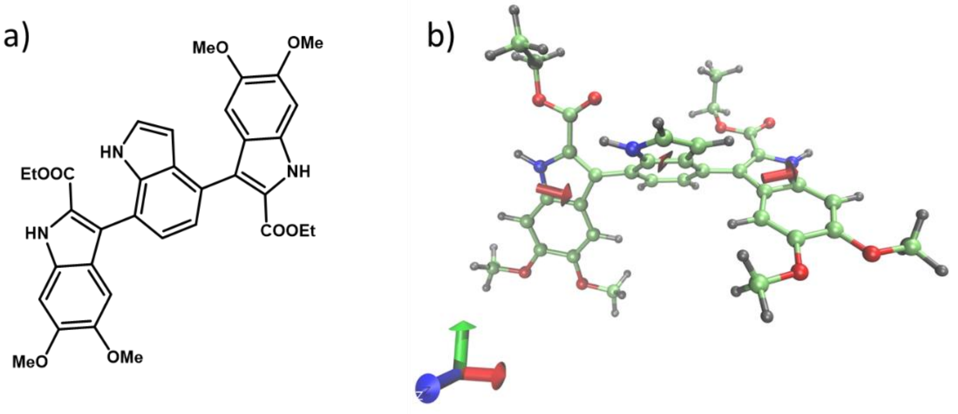

Figure S14: a) Structure and b) transition dipole moment in S_1 state for linear DMICE-T.

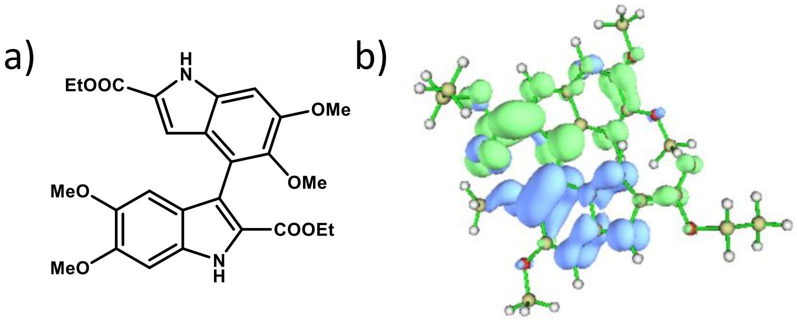

Figure S15: a) Structure and b) overlapped hole (blue) and electron (green) isosurface at the S_5 state of homodimer of DMICE.

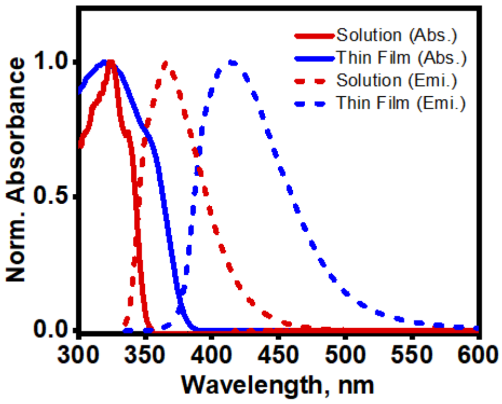

Figure S16: Normalized absorption and emission spectra of solution (blue lines) and thin film aggregates (red lines) of DMICE.

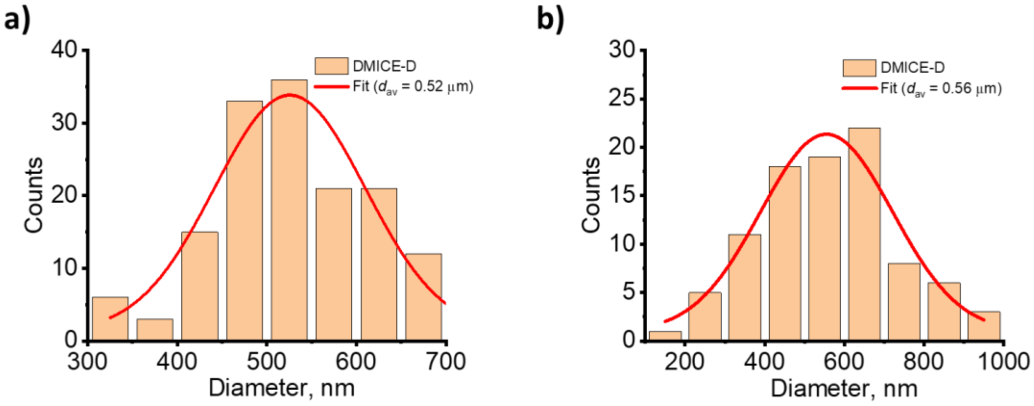

Figure S17: Histogram showing average size of DMICE-D aggregates in a) TEM and b) SEM.

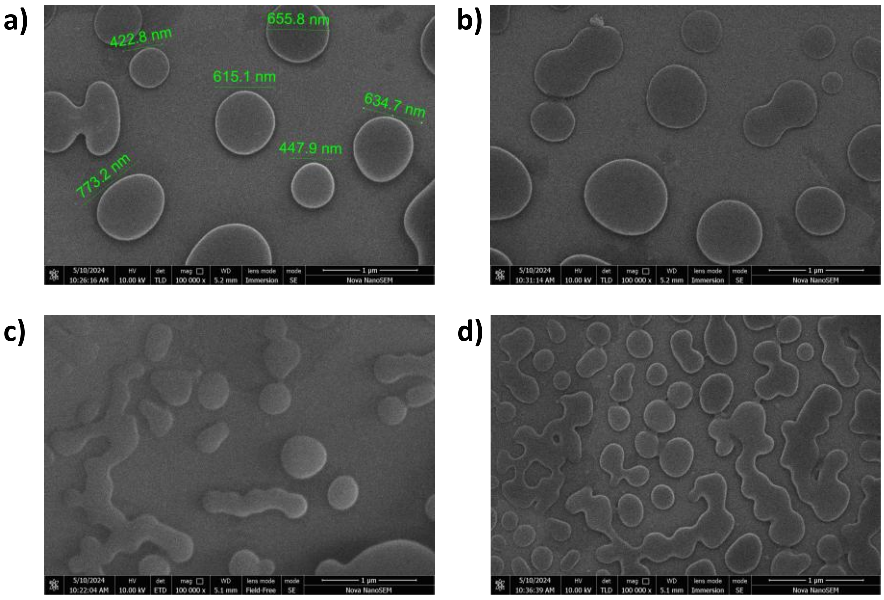

Figure S18: SEM images of DMICE-T showing distinct globular particles and elongated structures resulting from their assembly.

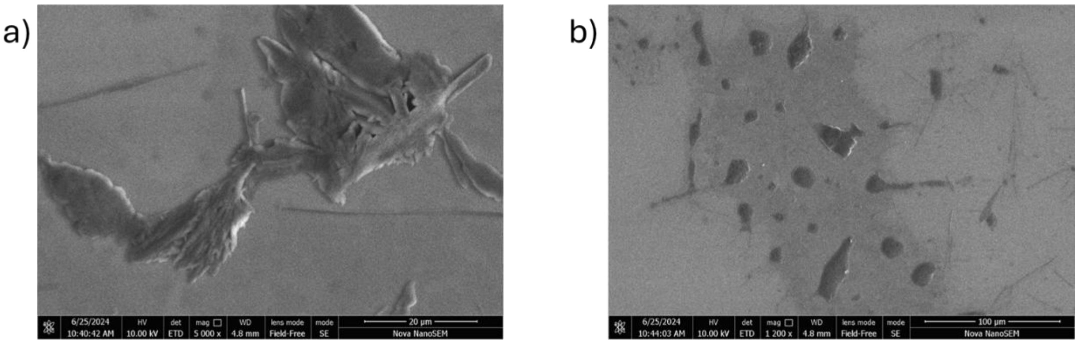

Figure S19: SEM images of DMICE aggregates showing lamellar morphology.

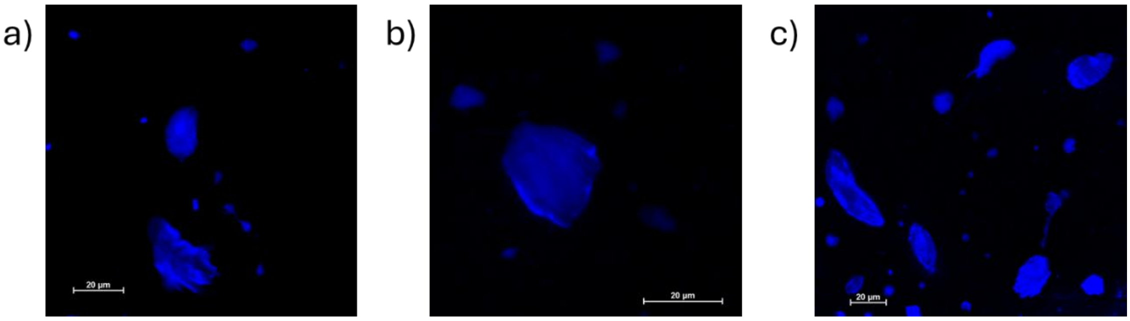

Figure S20: Confocal laser fluorescence microscopic images of DMICE aggregates showing lamellar morphology.

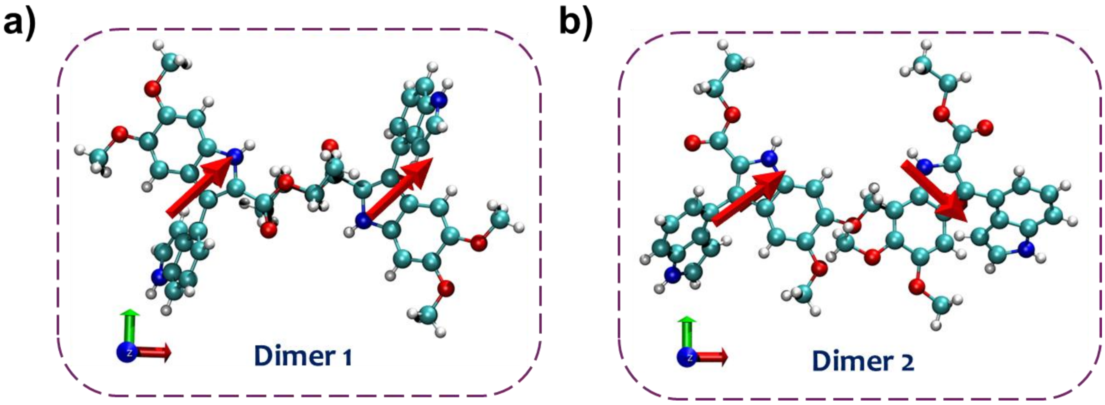

Figure S21: Two types of dimers within the crystal assembly of DMICE-D, named as a) DMICE-D1 and b) DMICE-D2, showing different transient dipole orientations.

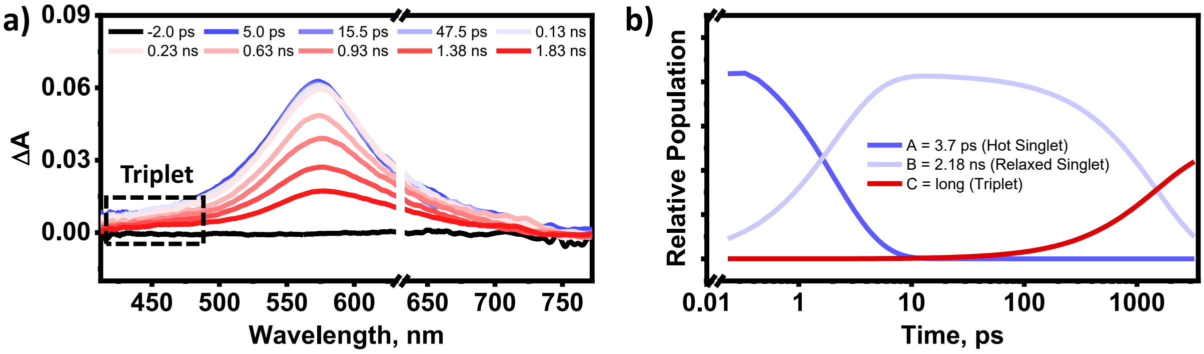

Figure S22: The fsTA spectra and corresponding deconvoluted time constants for DMICE-D in ACN.

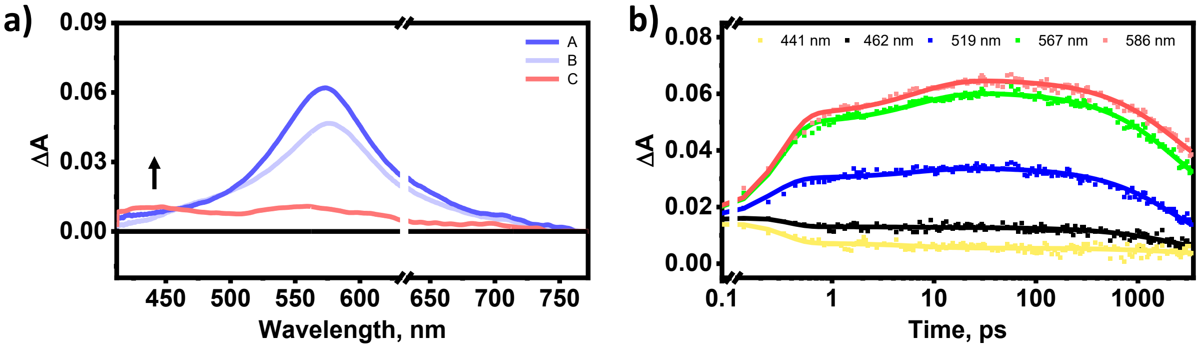

Figure S23: a) The evolution associated spectra (EAS) and b) the overlaid experimental versus fitted traces at different wavelengths for DMICE-D in TOL.

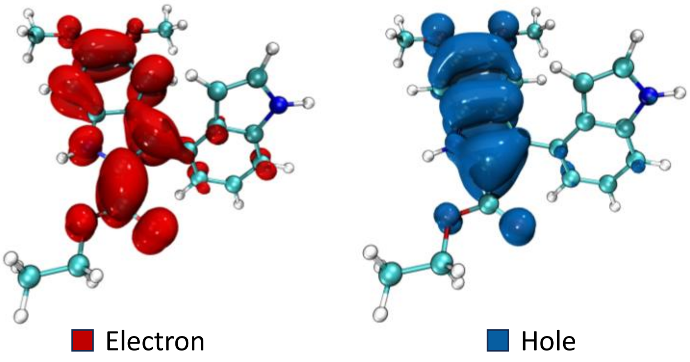

Figure S24: Electron and hole iso-surface plots of DMICE-D at the S_2 state.

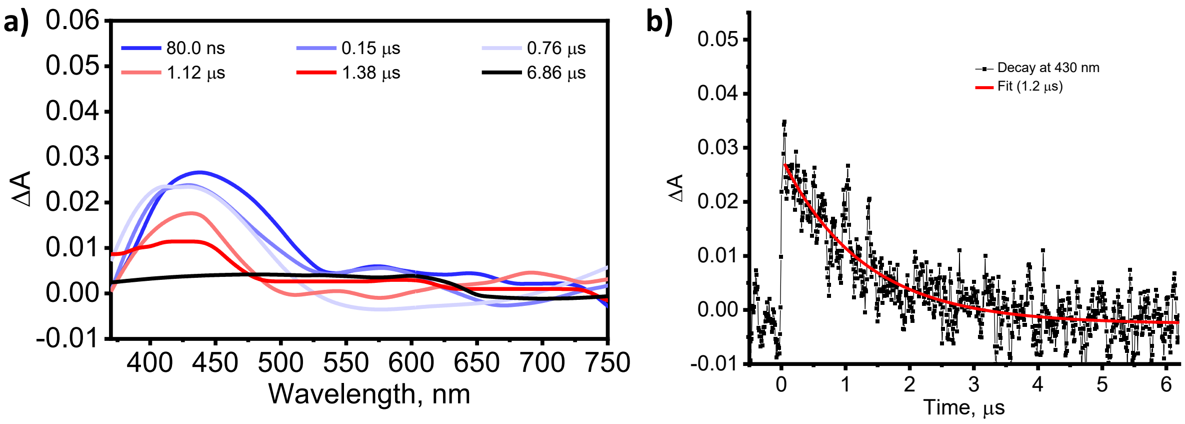

Figure S25: a) The nsTA spectra and b) decay trace at 440 nm for DMICE-D in TOL.

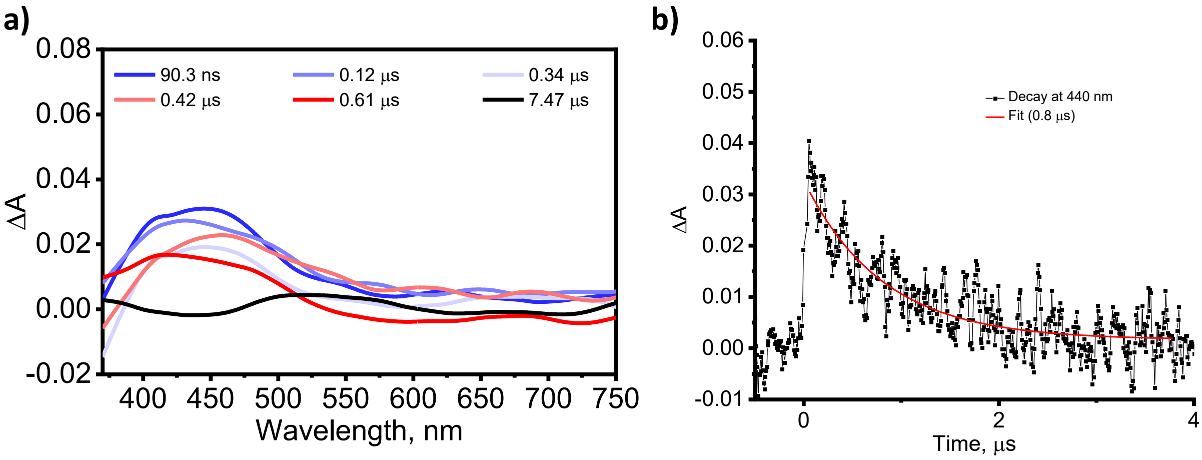

Figure S26: a) The nsTA spectra and b) decay trace at 440 nm for DMICE-D in ACN.

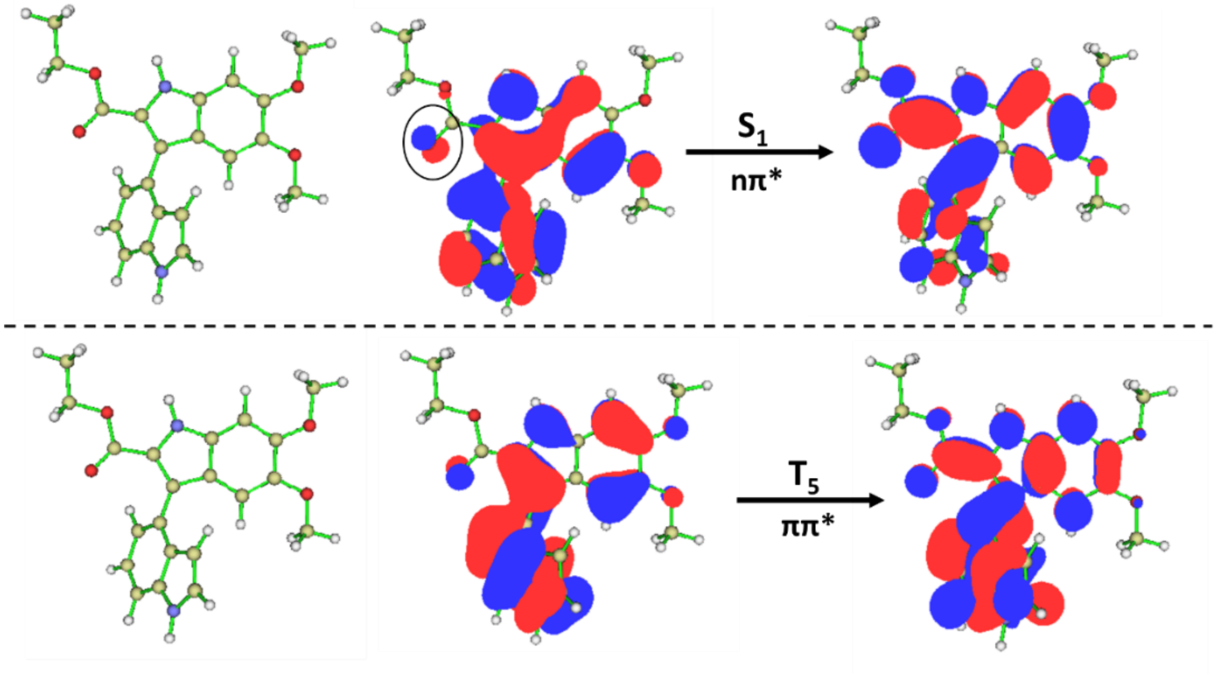

Figure S27: Natural transition orbitals (NTOs) of DMICE-D at the S_1 and T_5 states, showing the participation of non-bonding orbitals of the carbonyl group of the DMICE units for the S_1 state. Respective molecular orientation is shown on the left.

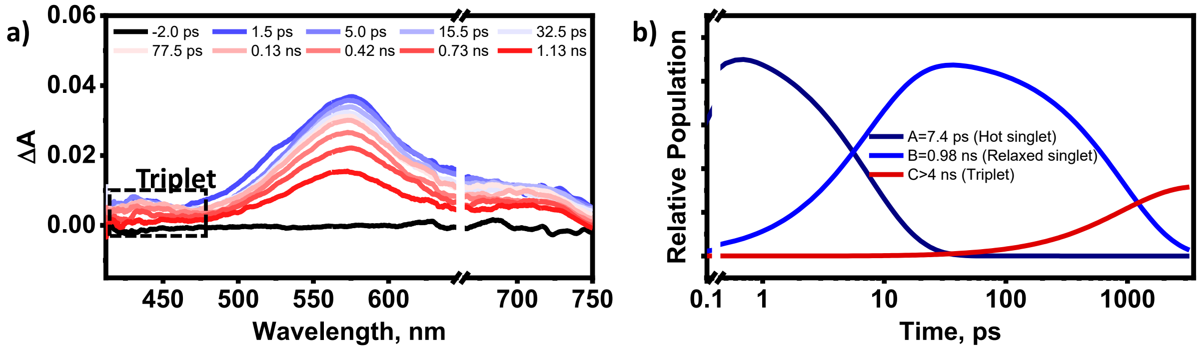

Figure S28: The fsTA spectra and corresponding deconvoluted time constants for DMICE-T in TOL.

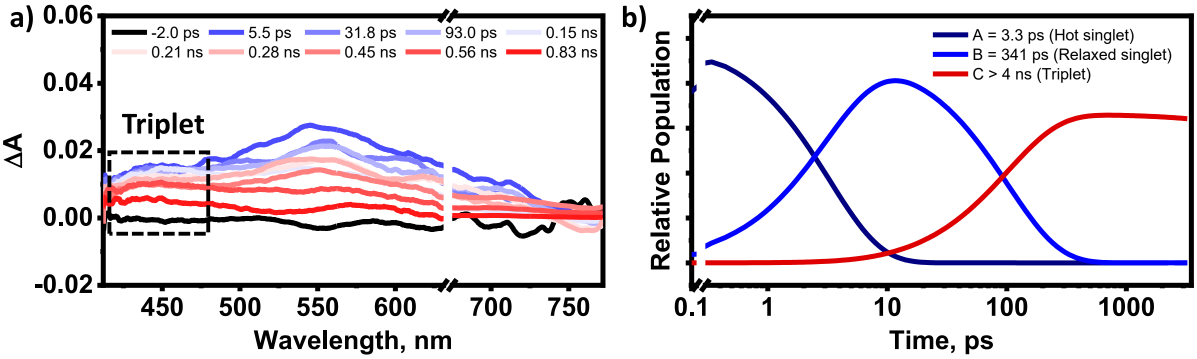

Figure S29: The fsTA spectra and corresponding deconvoluted time constants for DMICE-T in ACN.

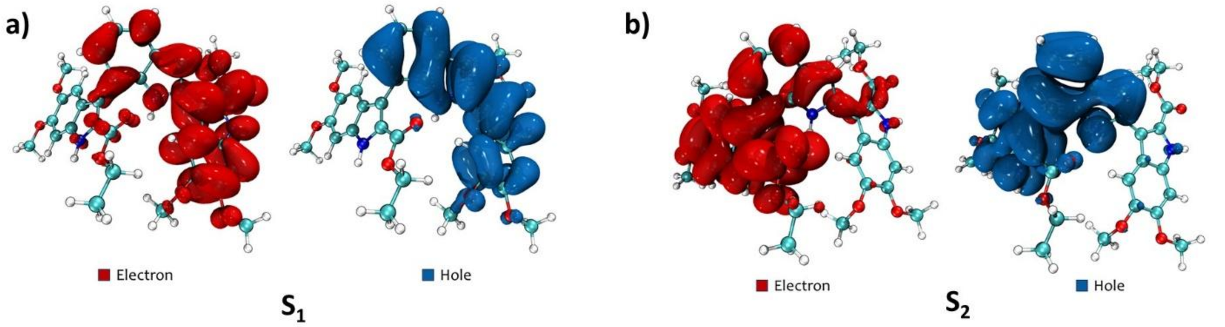

Figure S30: Electron and hole iso-surface plots of DMICE-T at the S_1 and S_2 states, showing CT character.

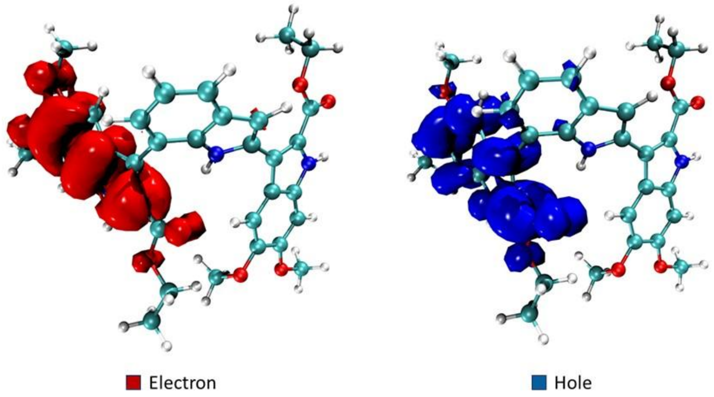

Figure S31: Electron and hole iso-surface plots of DMICE-T at the S_3 state, showing Frenkel exciton nature.

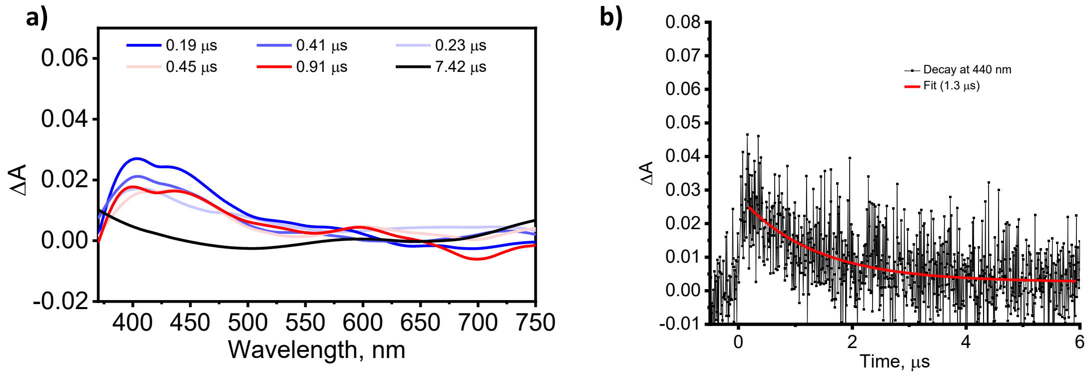

Figure S32: a) The nsTA spectra and b) decay trace at 440 nm for DMICE-T in TOL.

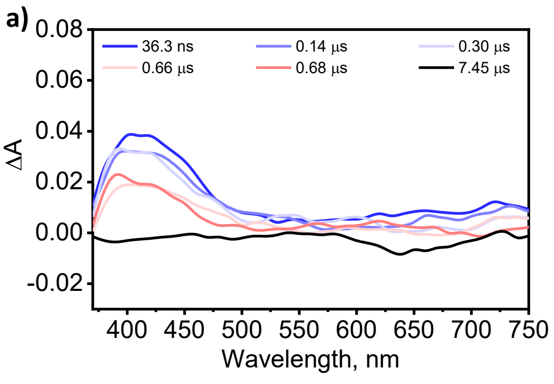

Figure S33: a) The nsTA spectra and b) decay trace at 440 nm for DMICE-T in ACN.

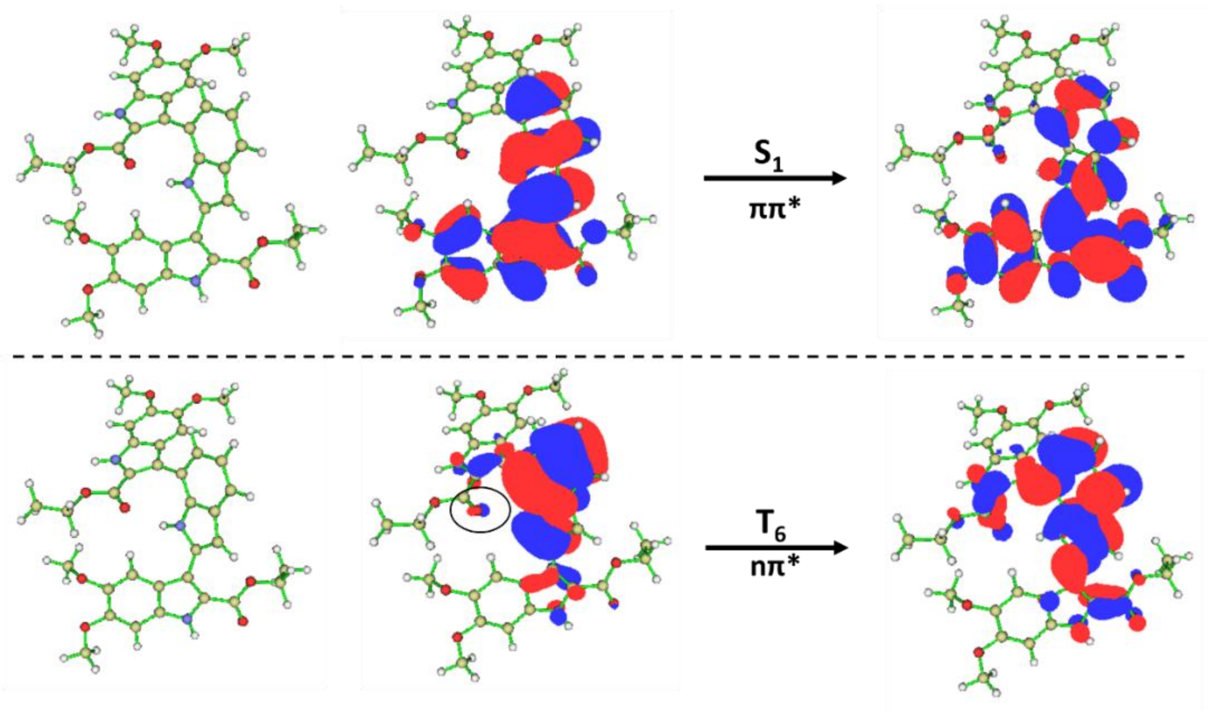

Figure S34: Natural transition orbitals (NTOs) of DMICE-T at the S_1 and T_6 states, showing the participation of non-bonding orbitals of the carbonyl group of the DMICE units for the T_6 state. Respective molecular orientation is shown on the left.

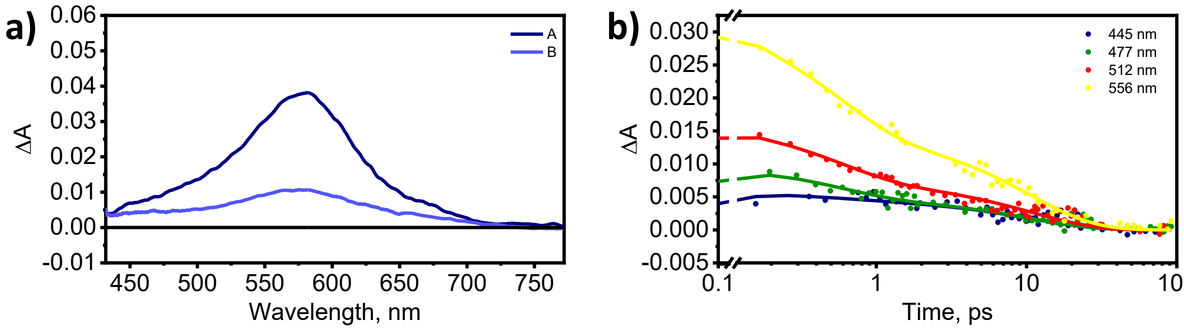

Figure S35: a) The evolution associated spectra (EAS) and b) the overlaid experimental versus fitted traces at different wavelengths for DMICE-D thin film.

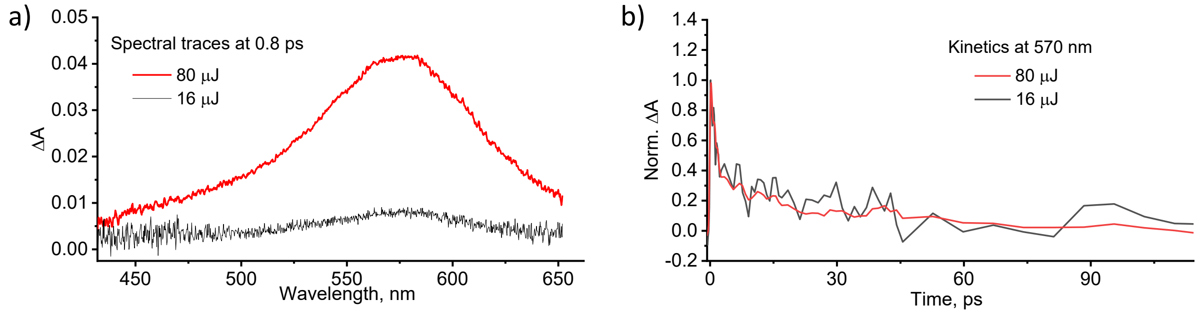

Figure S36: a) Spectral traces of DMICE-D thin film at 0.8 ps for different pump fluences; b) Normalized kinetic traces of DMICE-D thin film at 570 nm for different pump fluences.

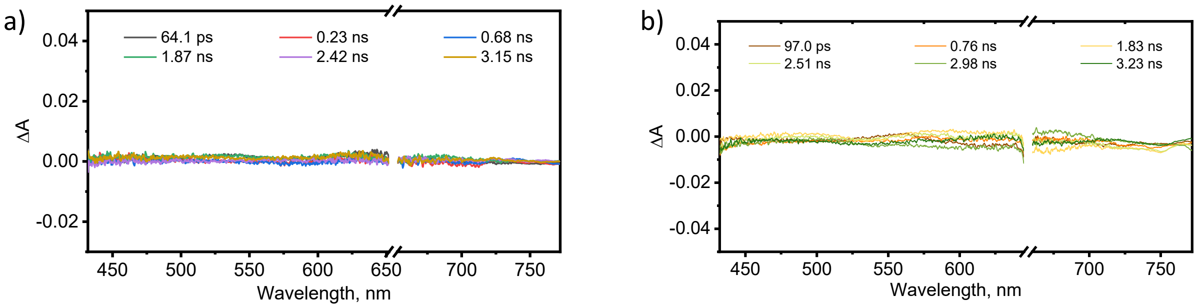

Figure S37: Transient absorption spectral traces of a) DMICE-D film and b) DMICE-T film beyond 50 ps.

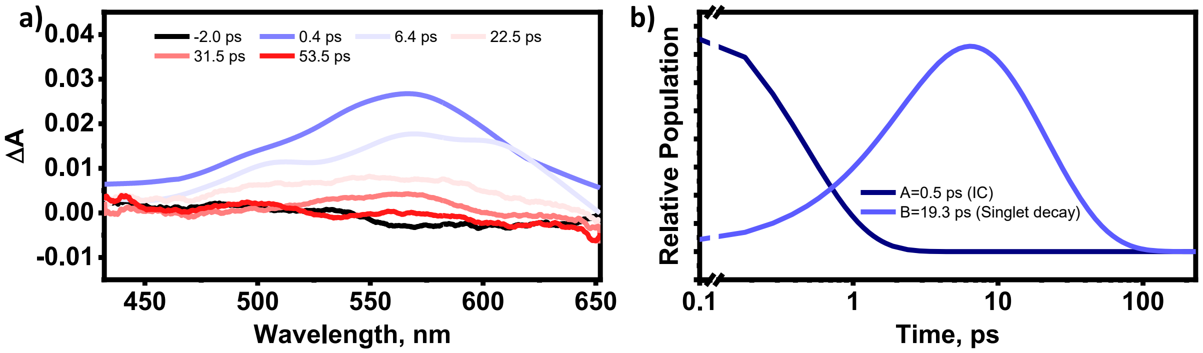

Figure S38: The fsTA spectra and corresponding deconvoluted time constants for DMICE-T thin film.

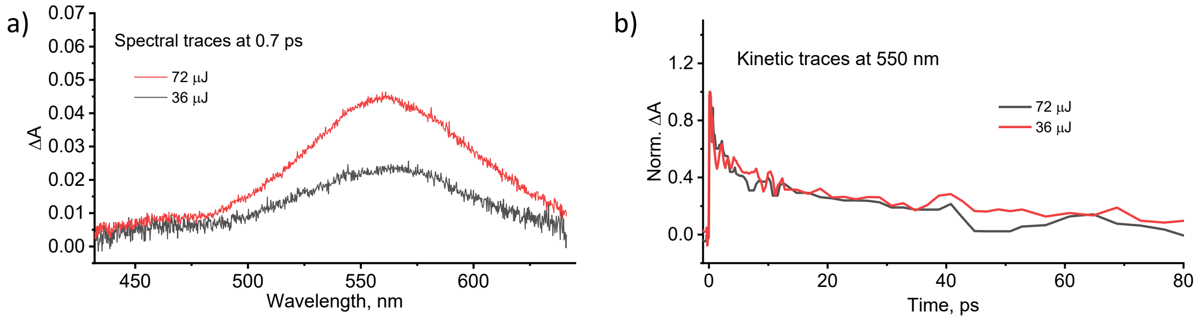

Figure S39: a) Spectral traces of DMICE-T thin film at 0.7 ps for different pump fluences; b) Normalized kinetic traces of DMICE-T thin film at 570 nm for different pump fluences.

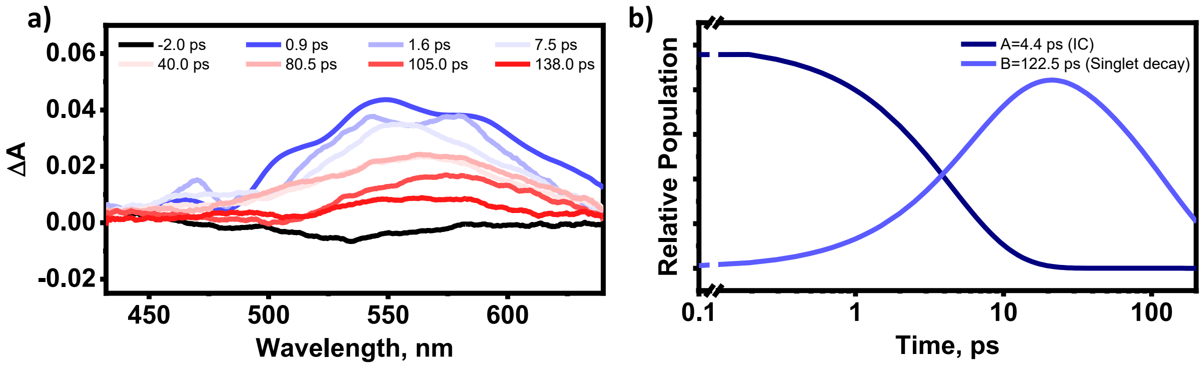

Figure S40: The fsTA spectra and corresponding deconvoluted time constants for DMICE thin film.

Section D: Appendix – Characterization Data

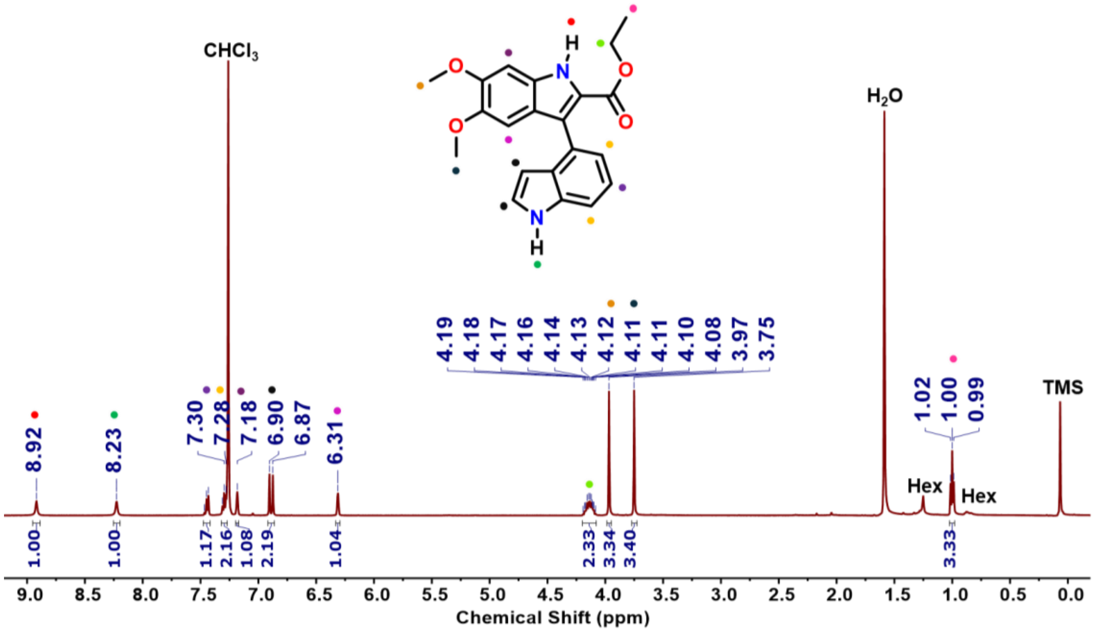

Figure A1: ^{1}H-NMR of DMICE-D in CDCl$_3$.

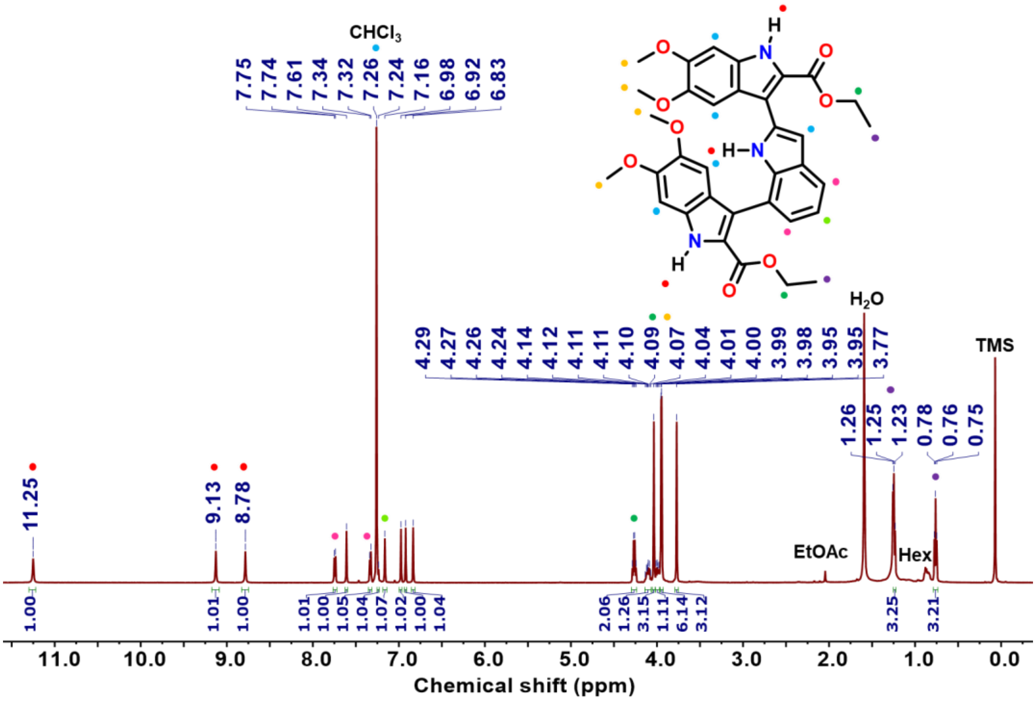

Figure A2: ^{1}H-NMR of DMICE-T in CDCl$_3$.

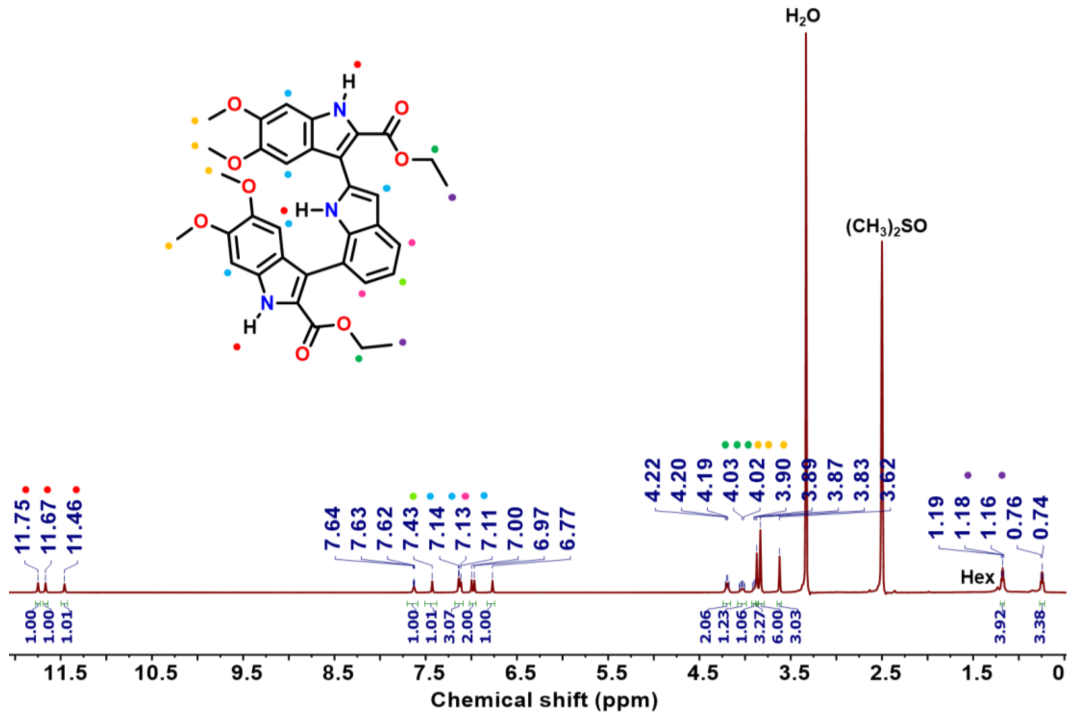

Figure A3: ^{1}H-NMR of DMICE-T in DMSO-d_6.

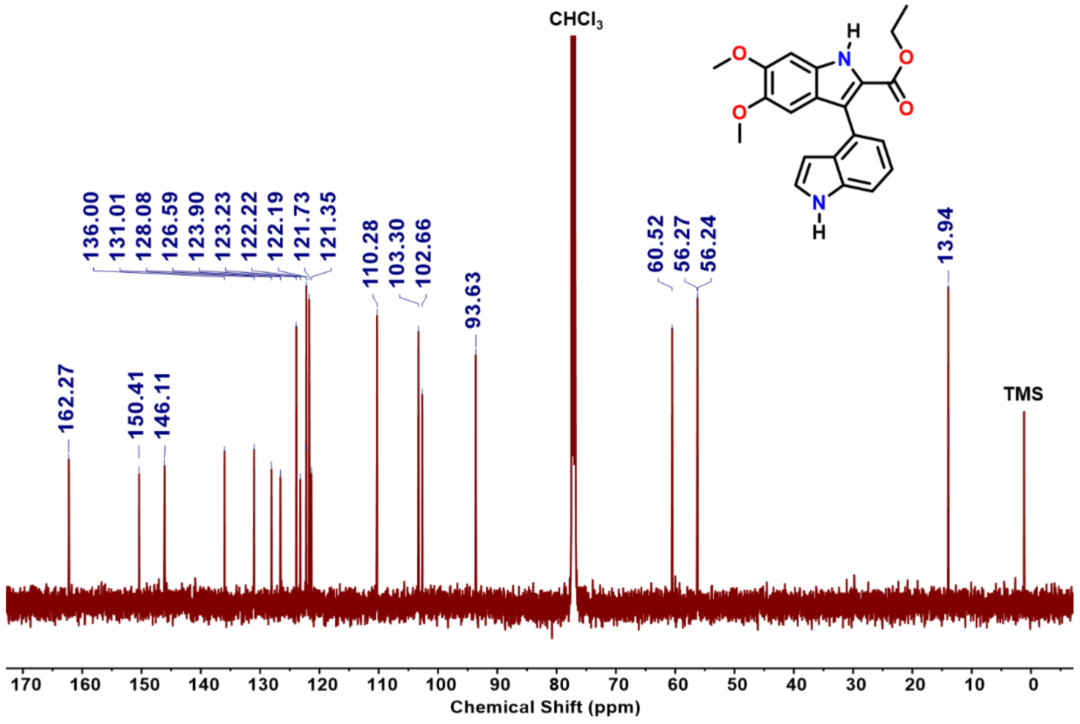

Figure A4: ^{13}C-NMR of DMICE-D in $CDCl_3$.

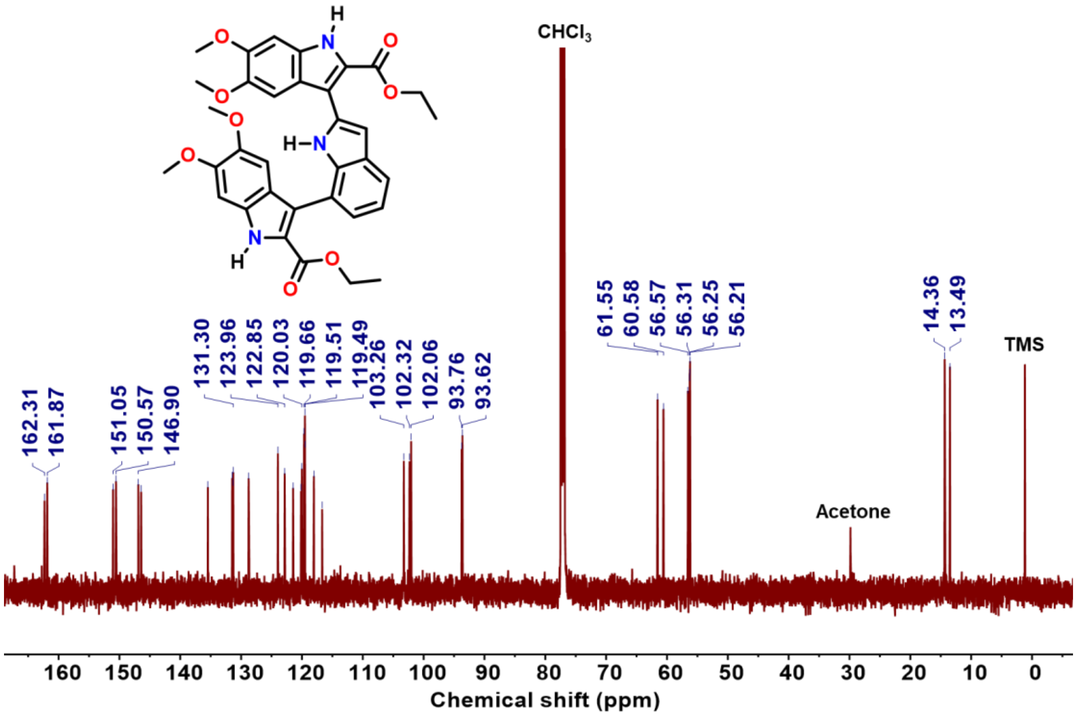

Figure A5: ^{13}C-NMR of DMICE-T in $CDCl_3$.

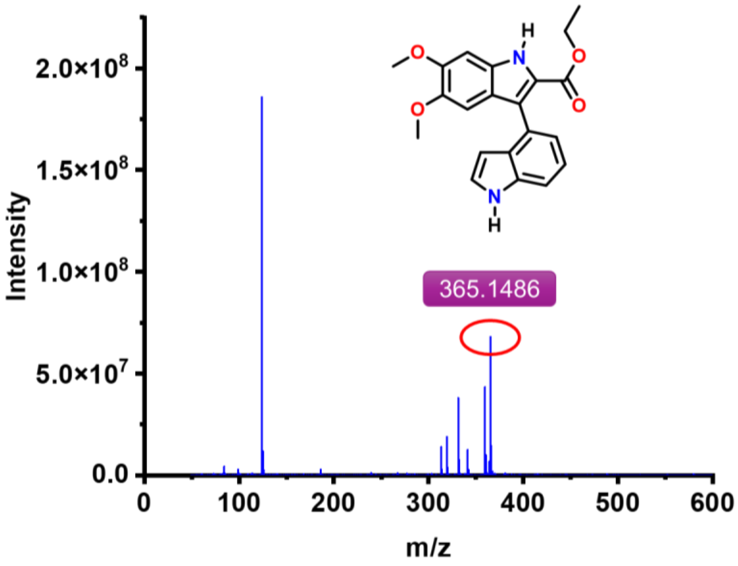

Figure A6: HRMS spectrum of DMICE-D.

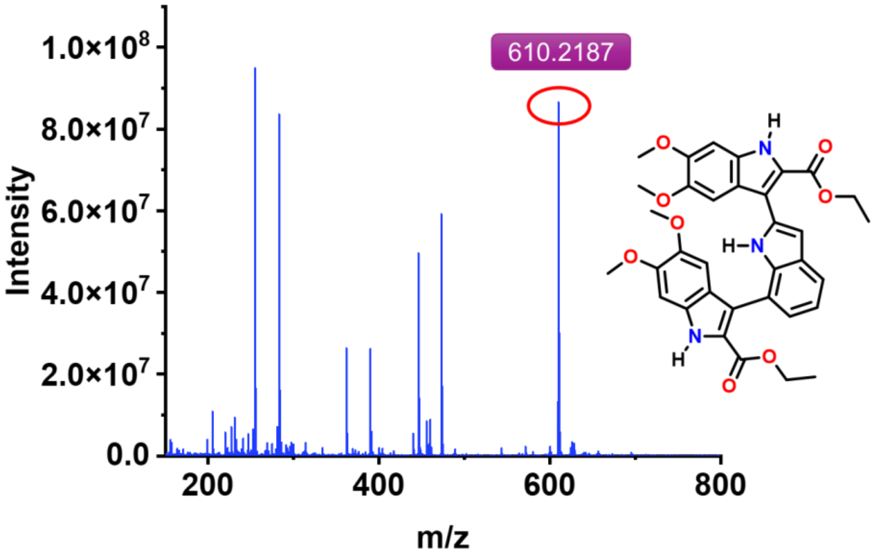

Figure A7: HRMS spectrum of DMICE-T.

References

1) Sheldrick, G. M., IUCr. **2007**, *64*, 112–122.
2) Farrugia, L. J.; IUCr. **1999**, *32*, 837–838.
3) Bruno, I. J.; Cole, J. C.; Edgington, P. R.; Kessler, M.; Macrae, C. F.; McCabe, P.; Pearson, J.; Taylor, R., **2002**, *58*, 389–397.
4) Gaussian 16, Revision C.01, M. J. Frisch, G. W. Trucks, H. B. Schlegel, G. E. Scuseria, M. A. Robb, J. R. Cheeseman, G. Scalmani, V. Barone, G. A. Petersson, H. Nakatsuji, X. Li, M. Caricato, A. V. Marenich, J. Bloino, B. G. Janesko, R. Gomperts, B. Mennucci, H. P. Hratchian, J. V. Ortiz, A. F. Izmaylov, J. L. Sonnenberg, D. Williams-Young, F. Ding, F. Lipparini, F. Egidi, J. Goings, B. Peng, A. Petrone, T. Henderson, D. Ranasinghe, V. G. Zakrzewski, J. Gao, N. Rega, G. Zheng, W. Liang, M. Hada, M. Ehara, K. Toyota, R. Fukuda, J. Hasegawa, M. Ishida, T. Nakajima, Y. Honda, O. Kitao, H. Nakai, T. Vreven, K. Throssell, J. A. Montgomery, Jr., J. E. Peralta, F. Ogliaro, M. J. Bearpark, J. J. Heyd, E. N. Brothers, K. N. Kudin, V. N. Staroverov, T. A. Keith, R. Kobayashi, J. Normand, K. Raghavachari, A. P. Rendell, J. C. Burant, S. S. Iyengar, J. Tomasi, M. Cossi, J. M. Millam, M. Klene, C. Adamo, R. Cammi, J. W. Ochterski, R. L. Martin, K. Morokuma, O. Farkas, J. B. Foresman, and D. J. Fox, Gaussian, Inc., Wallingford CT, **2016**.
5) J. S. Brown, “GitHub - JoshuaSBrown/QC_Tools: This small repository provides functionality for calculating the charge transfer integrals between two molecules.” can be found under https://github.com/JoshuaSBrown/QC_Tools, (accessed: (Apr 15, 2020)).
6) N. J. Hestand, F. C. Spano, *J. Chem. Phys.* **2015**, *143*, 244707.
7) N. J. Hestand, F. C. Spano, *Chem. Rev.* **2018**, *118*, 7069–7163.
8) T. Lu, F. Chen, *J. Comput. Chem.* **2012**, *33*, 580–592.
9) F. Plasser, *J. Chem. Phys.* **2020**, *152*, 084108.
10) F. Plasser, H. Lischka, *J. Chem. Theory Comput.* **2012**, *8*, 2777-2789.
11) A. Mohan, E. Sebastian, M. Gudem, M. Hariharan, *J. Phys. Chem. B* **2020**, *124*, 6867–6874.